PNAS RESEARCH ARTICLE | CHEMISTRY

Computational investigation of water glasses using machine-learning potentials

Ryan J. Szukalo[a], Nicolas Giovambattista[b], and Pablo G. Debenedetti[c,1]

Affiliations are included on p. 9.

Contributed by Pablo G. Debenedetti; received April 21, 2025; accepted July 2, 2025; reviewed by Thomas Loerting and Fausto Martelli

The molecular origins of water's anomalous properties have long been a subject of scientific inquiry. The liquid–liquid phase transition hypothesis, which posits the existence of distinct low-density and high-density liquid states separated by a first-order phase transition terminating at a critical point, has gained increasing experimental and computational support and offers a thermodynamically consistent framework for many of water's anomalies. However, experimental challenges in avoiding crystallization near the postulated liquid–liquid critical point have focused attention to water's canonical glassy states: low-density and high-density amorphous ice. Here, we use two Deep Potential machine-learning models, trained on the Strongly Constrained and Appropriately Normed density functional and the highly accurate Many-Body Polarizable potential, to conduct an investigation of water's glassy phenomenology based on quantum mechanical calculations. Despite not being explicitly trained on amorphous ices, both models accurately capture the structure and transformation of the water glasses, including their interconversion along different thermodynamic paths. Isobaric quenching of liquid water at various pressures generates a continuum of intermediate amorphous ices and density fluctuations increase near the liquid–liquid critical pressure. The glass transition temperatures of the amorphous ices produced at different pressures exhibit two distinct branches, corresponding to low-density and high-density amorphous ice behaviors, consistent with experiment and the liquid–liquid transition hypothesis. Extrapolating transformation pressures from isothermal compressions to experimental compression rates brings our simulations into excellent agreement with data. Our findings demonstrate that machine-learning potentials trained on equilibrium phases can effectively model nonequilibrium glassy behavior and pave the way for studying long-timescale, out-of-equilibrium processes with quantum mechanical accuracy.

water | molecular dynamics | machine-learning | Deep Potential | glasses

Significance

Water's anomalous properties have long intrigued scientists. One explanation is the existence of two metastable liquid states at low temperatures and elevated pressures, separated by a first-order phase transition. Experimental confirmation remains difficult due to rapid ice formation, making glassy phases central to studying cold, noncrystalline water. We use machine-learning potentials with molecular dynamics simulations to conduct an investigation of water glasses based on quantum mechanical calculations. The models accurately reproduce experimental observations of low- and high-density amorphous ices without being explicitly trained on them. Our findings support the liquid–liquid phase transition hypothesis and suggest experimental pathways for probing criticality by quenching water near the proposed critical pressure, where enhanced density fluctuations may persist in the glassy state.

Water, an essential and extensively studied substance, continues to interest scientists on account of its distinctive behavior (1). Its numerous anomalous properties, such as the density maximum at 4 °C at ambient pressure and the sharp increases in compressibility and heat capacity upon cooling, have attracted the interest of researchers for decades (2–4). Efforts to uncover the molecular origins of these anomalies have produced several theoretical frameworks, including the stability-limit conjecture (5), the singularity-free scenario (6), and the liquid–liquid phase transition (LLPT) hypothesis (7). Among these, the LLPT hypothesis has garnered substantial computational (8–12) and experimental (13–18) support. It posits that supercooled water at low temperatures and moderate superatmospheric pressures can exist in two distinct liquid states: a low-density liquid (LDL) and a high-density liquid (HDL), separated by a first-order phase transition line that terminates at a liquid–liquid critical point (LLCP) (7, 19).

The definitive experimental validation of the LLPT has proven challenging because water rapidly crystallizes in the deeply supercooled regime, complicating the direct observation of the hypothesized LLCP (20). This challenge has motivated significant focus on water's glassy states. Mishima et al. first demonstrated that water could exist in at least two amorphous forms: low-density amorphous (LDA) and high-density amorphous (HDA) ice (21, 22). These glassy states are hypothesized to be the amorphous solid analogs of LDL and HDL (20). In 2001, Loerting et al. demonstrated that by heating HDA at high pressures (11 to 19 kbar), an ≈9% more dense amorphous state called very high-density amorphous ice (vHDA), could be generated (23). More recently, Rosu-Finsen et al. found a new amorphous state, medium density amorphous ice (MDA), formed by ball milling ice Ih at 77 K (24). In this work, we do not consider

Author contributions: R.J.S., N.G., and P.G.D. designed research; R.J.S. performed research; R.J.S., N.G., and P.G.D. analyzed data; and R.J.S., N.G., and P.G.D. wrote the paper.

Reviewers: T.L., Universitat Innsbruck; and F.M., Istituto dei Sistemi Complessi Consiglio Nazionale delle Ricerche.

The authors declare no competing interest.

[1]To whom correspondence may be addressed. Email: pdebene@princeton.edu.

This article contains supporting information online at https://www.pnas.org/lookup/suppl/doi:10.1073/pnas.2509609122/-/DCSupplemental.

Published August 5, 2025.

shear-generated glasses. An increasingly rich literature exists on the structural and dynamic properties of the various amorphous states, although computational characterization has been largely limited to LDA and HDA. Thus we restrict our focus to only these two glasses in this work.

Experimentally, LDA can be produced by condensation of water vapor onto cold substrates (25) or by hyperquenching liquid water at atmospheric pressure with cooling rates of at least 10^6 K/s (10^{-3} K/ns), which are required to bypass crystallization (26, 27). HDA can be generated in a variety of manners, most commonly by isothermal compression of hexagonal ice (21, 28). Hyperquenching the liquid under pressure (5 kbar) also produces HDA (29). Notably, LDA and HDA can be interconverted via isothermal compression or decompression, exhibiting characteristics that one can associate with a metastable first-order phase transition (21, 30, 31).

The connection between amorphous ices (LDA/HDA) and the LLPT hypothesis is rooted in the concept that these glassy states are the arrested, nonequilibrium analogs of their corresponding supercooled liquid counterparts (LDL/HDL). When rapidly cooled below their glass transition temperatures, these liquid phases are hypothesized to transform into their respective amorphous solid forms, preserving key structural signatures. This relationship has long suggested that studying the transitions between LDA and HDA can provide evidence for the existence of an LLPT in the otherwise experimentally difficult to sample deeply supercooled liquid regime. These glassy states thus provide an important experimental link to the LLPT hypothesis, bridging theory and observation and offering a unique window into water's anomalous behavior (32, 33).

Molecular simulations have proven invaluable for investigating the glassy landscape. Extensive studies using classical atomistic models such as ST2 (34–36), TIP4P/2005 (37–39), and SPC/E (40); as well as a machine-learned coarse-grained model, ML-BOP (41–44), have shed light on the relationship between LDA and HDA. While these models qualitatively reproduce various structural and thermodynamic properties of LDA and HDA, their predictions can vary depending on the presence(or lack thereof) of an accessible LLCP. Giovambattista et al. demonstrated that for the ST2 model, which exhibits an LLCP, the glass transition temperatures $T_g(P)$ strongly depend on the glass preparation path (45). In contrast, for the SPC/E model, which lacks an accessible LLCP, the $T_g(P)$ values for different glassy states collapse onto a single curve regardless of their preparation history (45). These path-dependent behaviors in ST2 are consistent with experimental observations (46). Recent studies with TIP4P/2005 by Gartner et al. revealed complementary evidence through observing an increase in long-range density fluctuations in the glasses formed near the critical pressure. Such features are absent in mW water, which lacks an LLCP despite showing both positively and negatively slopped $T_g(P)$ behavior (47). Despite these valuable insights from classical models, they remain limited by their empirical parameterizations, highlighting the need for more fundamental approaches to understanding water's complex glassy behavior.

Ab initio molecular dynamics (AIMD), in which the electronic structure and interatomic forces are calculated with quantum accuracy at each step in the simulation, offers a more rigorous framework for studying molecular systems, but is often limited by its high computational cost (48, 49). Although advances in computational hardware have enabled calculations involving larger systems and longer time scales, the characteristic times required to probe glassy behavior and polyamorphic transitions between deeply supercooled or glassy phases remain largely beyond the reach for AIMD. Recent, important progress involving machine-learning potentials (MLPs) has bridged this gap, combining the accuracy of quantum mechanical calculations with the efficiency required for extensive molecular dynamics simulations (50–52). This approach has ushered in a new era of exploration of water's complex low-temperature, metastable behavior (53).

In this work, we use one such MLP simulation method, Deep Potential Molecular Dynamics (DPMD), to conduct an investigation of water's glassy phenomenology based on density functional theory (DFT) and quantum mechanical calculations (51, 54). The Deep Potential (DP) method uses neural networks to learn the mapping between atomic environments and potential energy, preserving essential symmetries while efficiently representing the complex many-body physics of the underlying system (55). To represent the DFT potential energy surface, we use the Strongly Constrained and Appropriately Normed (SCAN) exchange correlation functional (56). SCAN has been shown to accurately represent several of water's properties (57, 58) and SCAN based DP models have been used to investigate water phase-equilibria (59–62) and autoionization (63).

To efficiently sample the SCAN-based potential energy surface, we use a previously trained DP model, referred to here as DP_SCAN, which accurately reproduces key features of water's complex phase diagram from ambient conditions to approximately 2000 K and 500 kbar (64). Additionally, we use a second DP model trained on the Many-Body Polarizable (MBpol) water model (65–67), referred to here as DP_MBpol. MBpol is widely recognized as the most accurate model of water's condensed phases available to date. This DP_MBpol model was trained to reproduce the low-pressure region of water's phase diagram (up to 10 kbar), successfully capturing the stability regions of ice Ih, II, III, V, and VI polymorphs in quantitative agreement with experiment (68). However, a critical question remains: Can MLPs trained primarily on equilibrium liquid and crystalline phases accurately represent complex, out-of-equilibrium states like amorphous ices? Addressing this question has implications not only for our understanding of water's complex behavior but also for the broader application of MLPs to materials science.

By using MLPs trained on DFT (SCAN) and MBpol, we explore the glassy landscape of water and test the validity of these models beyond their original training datasets. Our findings demonstrate that these models accurately capture the physics of glassy water, consistent with the LLPT scenario, while validating prior studies based on classical models. These results not only reinforce the LLPT/LLCP picture as a cornerstone for understanding water's anomalies but also establish that carefully constructed MLPs can successfully extrapolate to predict complex, nonequilibrium phenomena even when trained primarily on equilibrium states.

Results

Hyperquenching Liquid Water at 1 bar Generates LDA. Low-density amorphous ice can be experimentally generated by rapidly quenching liquid water at ambient pressure (26, 27). To replicate this process computationally, isobaric quenching simulations were performed with a constant cooling rate of $q_c = 1$ K/ns at $P = 1$ bar using the DP_SCAN and DP_MBpol models. This cooling rate is approximately 2 orders of magnitude faster than the fastest experimental quenching rates of 0.01 K/ns used

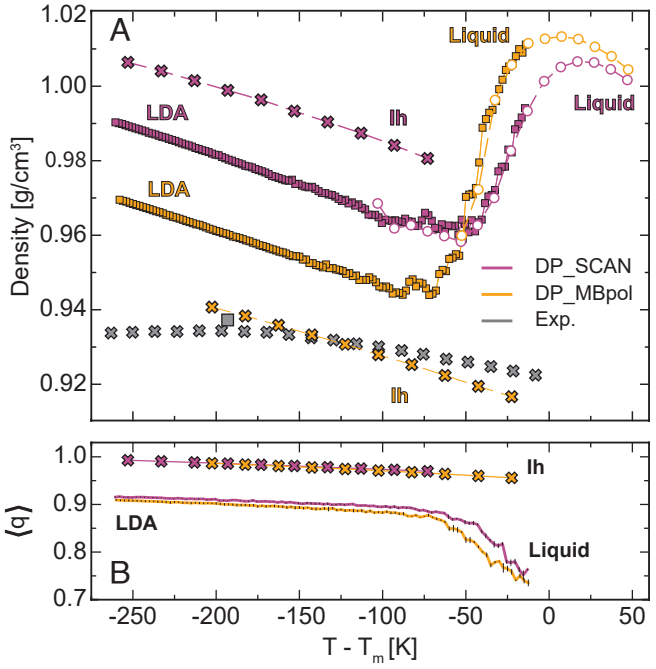

Fig. 1. Average density (*A*) and tetrahedral order parameter $\langle q \rangle$ (*B*) versus temperature, at atmospheric pressure, relative to each model's melting point ($T - T_m$). Quenching data are from isobaric simulations at $P = 1$ bar with a cooling rate of $q_c = 1$ K/ns [squares in (*A*), lines in (*B*)] while circles and crosses correspond to equilibrium liquid and ice Ih, respectively. Quenching data are averages of three independent runs. Purple and orange data represent DP_SCAN and DP_MBpol potentials, respectively. Gray symbols present experimental results for ice Ih (crosses) and LDA (square) at $T = 80$ K ($T - Tm = -193.1$ K) (70, 71).

to prepare LDA (69), but represents the slowest rate feasible for the DPMD simulations given the computational cost. Previous computational studies have demonstrated that the structural and thermodynamic properties of simulated water glasses are relatively insensitive to varying cooling rates (37, 41). Wong et al. (37) showed that reducing the cooling rate from 1 K/ns to 0.1 K/ns in TIP4P/2005 simulations produced only minor density differences (<0.01 g/cm^3) in the resulting LDA. *SI Appendix*, Fig. S4 demonstrates that results obtained at cooling rates of 1 K/ns and 10 K/ns show only slight density variation in the DPMD generated LDA, supporting the reliability of the simulated glasses despite the necessarily accelerated cooling process.

Fig. 1 provides a thermodynamic and structural characterization of these quenches and compares the results to equilibrium simulations of liquid water. Equilibrium simulations of ice Ih are also shown. Fig. 1*A* confirms the well-known fact that both models exhibit a density maximum slightly above their respective melting temperatures, followed by a rapid decrease in density as temperature decreases. This sharp decline in density matches the equilibrium liquid simulations and culminates at a density minimum whereafter the liquid falls out of equilibrium and forms a glassy phase. Low-temperature configurations where the density increases linearly with decreasing temperature correspond to LDA.

Notable differences emerge between the two models at low temperatures. Cryoflotation experiments reveal that the density of LDA (0.937 g/cm^3) is slightly greater than that of ice Ih (0.932 g/cm^3) at $T = 80$ K (70, 71). Fig. 1*A* shows that the DP_SCAN model incorrectly predicts this relationship, where the density of ice Ih is greater than that of LDA (21, 46). Conversely, the DP_MBpol model predicts the correct qualitative relationship, but overestimates the magnitude of the density difference compared to the experiments. These density differences may be addressed by including nuclear quantum effects (NQEs), as recent work by Eltareb and coworkers shows that the inclusion of NQEs for a classical water model can lower the LDA density by ≈0.04 g/cm^3 and correctly predict the change in slope of the temperature dependence of ice Ih upon cooling (72, 73).

Fig. 1*B* examines the structural basis of these density differences through the average tetrahedral order parameter (74, 75), $\langle q \rangle$, as a function of temperature. The ice Ih phases produced by both models show nearly identical local tetrahedral structures, as evidenced by consistent $\langle q \rangle$ values (crosses). While the LDA generated by the DP_SCAN model exhibits slightly enhanced tetrahedrality with respect to DP_MBpol, the differences are minimal, suggesting comparable local environments. This indicates that the density discrepancies between ice Ih and LDA cannot be attributed to variations in local tetrahedrality.

Near ambient temperatures, both models correctly predict that liquid water is denser than ice Ih, though the DP_SCAN model predicts a smaller density difference (≈4% for DP_SCAN versus ≈11% for DP_MBpol at the temperature of maximum density) whereas the experimental difference is approximately ≈10% (76). The SCAN functional is known to overestimate hydrogen bond strength in the condensed phase, which explains the higher predicted densities relative to experiments (58). While past studies with DFT-based MLPs comparing ice and liquid water have focused on the vicinity of the melting point (59, 60), our work reveals that at supercooled temperatures, this overestimation of hydrogen bond strength leads to qualitatively incorrect behavior such that LDA becomes less dense than ice Ih. This observation warrants further study into the impact of hydrogen bond strength on density upon supercooling, particularly within the context of DFT functionals and MLPs.

Fig. 2 demonstrates the structural fidelity of simulated LDA from both models compared to experimental data (77, 78). While the oxygen–oxygen radial distribution functions (RDFs)

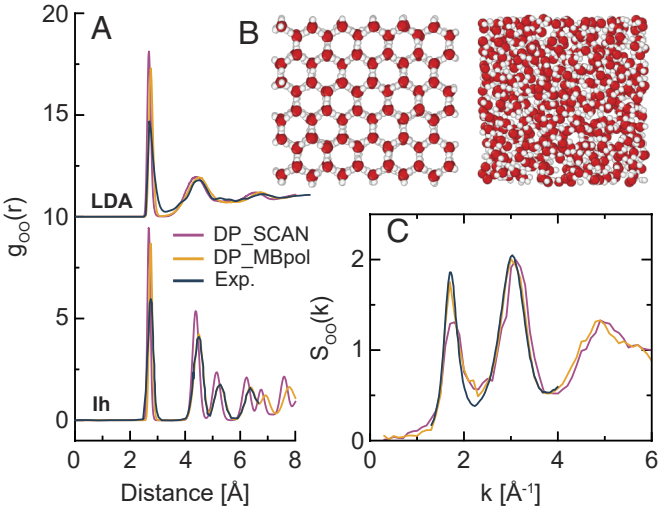

Fig. 2. Structural characterization of LDA generated using the DP_SCAN (purple) and DP_MBpol (orange) models compared with experimental data (black) (77, 78). (*A*) Oxygen–oxygen radial distribution functions, (*B*) representative snapshots of the atomic configurations generated by the DP_SCAN model for ice Ih (*Left*) and LDA (*Right*) at $T = 80$ K, and (*C*) Oxygen–oxygen structure factors.

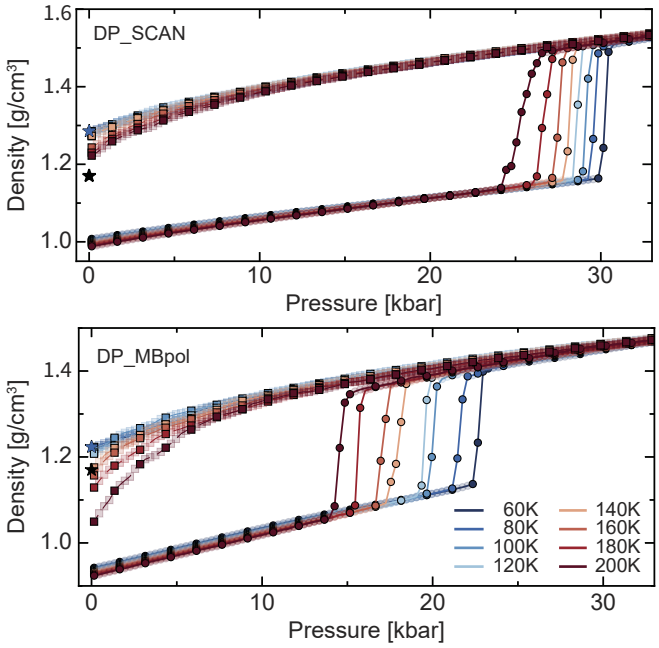

Fig. 3. Density versus pressure isotherms for the ice Ih to HDA compression (circles) and corresponding HDA decompression (squares) to ambient pressure. The *Top* and *Bottom* panels present results for the DP_SCAN and DP_MBpol models, respectively. All simulations employ a compression/decompression rate of q_p = 3,000 bar/ns. Recovered HDA densities at ambient pressure and T = 80 K (1.28 g/cm^3 for DP_SCAN and 1.22 g/cm^3 for DP_MBpol) are compared to the experimental value (1.15 g/cm^3) (22, 71), shown as blue and black stars, respectively. Data represent averages over three independent simulations while translucent and solid symbols are used only for visual purposes.

show overstructuring relative to experiment (black curves), this deviation is largely due to missing nuclear quantum effects (72). Both models successfully capture the distinctive structural signatures of LDA and ice Ih, with DP_SCAN exhibiting RDF maxima at slightly shorter distances than DP_MBpol, consistent with the observed density differences. The long-range order, as characterized by the small k behavior of the oxygen–oxygen static structure factor shown in Fig. 2*C* is well reproduced, with DP_MBpol achieving near-quantitative agreement with experimental measurements.

Despite the qualitative error in the DP_SCAN model regarding the ice Ih density relative to LDA, both models generate accurate representations of the LDA glasses themselves. The structural characteristics of the simulated glasses closely align with experimental observations, with densities within 4% of the experimental LDA density of 0.94 g/cm^3 (22, 46). This is particularly significant given that neither model was trained on LDA structures, indicating that these DP MLPs can reliably capture the essential physics of the LDA state.

Isothermal Compressions of Ice Ih and LDA Generate HDA. High-density amorphous ice (HDA) is commonly generated through isothermal compression of either ice Ih or LDA (21, 28, 30). We first focus on the compression of ice Ih to HDA, followed by decompression to recovered HDA at ambient pressure (1 bar).

Fig. 3 presents the density isotherms for both the DP_SCAN and DP_MBpol models under a compression and decompression rate of q_p = 3,000 bar/ns. This rate is approximately 10 orders of magnitude faster than the experimental compression rate used to study water glasses (21, 31), however the rates employed here are consistent with previously used computational rates (34, 40, 45). Moreover, rates similar to those used here and other computational water glass studies can be achieved experimentally (79) and these fast compression rates have been used to study the freezing of water under compression (80, 81). The ice to HDA transitions are notably sharp, consistent with prior results from both classical models (37, 38, 40) and experimental studies (19, 22, 30). However, the transition pressures are significantly higher than those observed experimentally, due to the much faster compression rates used in simulations compared to experiments (simulations using slower compression/decompression rates and extrapolation to experimental rates are discussed below).

However, rate effects alone may not be able to fully explain the discrepancy. Our simulations employed pristine monocrystalline ice Ih, which lacks the grain boundaries and defects present in experimental samples. Recent computational studies demonstrate that polycrystalline ice amorphizes at pressures up to 40% lower than monocrystalline ice due to heterogeneous nucleation at grain boundaries (41), providing a mechanistic explanation for the higher transition pressures observed in our simulations. Additionally, Eltareb and coworkers demonstrated that the inclusion of NQEs also reduced the ice Ih to HDA transition pressure (73).

Recovered HDA densities at ambient pressure and T = 80 K (1.28 g/cm^3 for DP_SCAN and 1.22 g/cm^3 for DP_MBpol) overestimate the corresponding experimental density (1.15 g/cm^3) (22, 71), with DP_SCAN producing a denser HDA compared to DP_MBpol. We note, however, that the density of recovered HDA at 1 bar can vary slightly with the pressure of HDA before decompression (e.g., the density of HDA recovered from P = 1,500 MPa may be slightly lower (at 1 bar) than the corresponding density of HDA recovered from 2,000 MPa) (40).

Fig. 4 presents the corresponding isotherms for the LDA to HDA transition, under a compression and decompression rate of q_p = 3,000 bar/ns. Panels (*A* and *C*) illustrate the compression of LDA to HDA at temperatures ranging from 60 K to 200 K for the DP_SCAN and DP_MBpol models, respectively. Consistent with classical models and experimental observations, the LDA to HDA transition occurs at lower pressures relative to the Ih to HDA transition (34, 38, 82). The transition is again quite sharp and it occurs at lower pressures as the temperature increases, suggestive of an underlying first-order phase transition (83), supporting the hypothesis that LDA and HDA are the glass counterparts to LDL and HDL.

Inset panels (Fig. 4 *B* and *D*) highlight the behavior of HDA upon decompression to negative pressures. The density decreases monotonically as the pressure becomes more negative, reflecting the instability of HDA and transition to LDA. Notably, the DP_SCAN model (Fig. 4*B*) shows a clear transition back to LDA before the amorphous ice fractures (at very negative pressures), as evidenced by a distinct change in the slope of the density-pressure curve. This change in slope allows for an estimate of the HDA to LDA transition pressure (see *SI Appendix*, Fig. S3 for details). This transition is less apparent in the DP_MBpol model (Fig. 4*D*), where the density smoothly shifts from HDA-like to LDA-like without a sharp transition, thus preventing an estimate of the HDA to LDA transition pressure. As alluded to previously, the decompression rates employed in this study are orders of magnitude larger than those used in experiments—so these results may be sensitive to the compression rate used. As demonstrated in *SI Appendix*, Fig. S5, these differences between

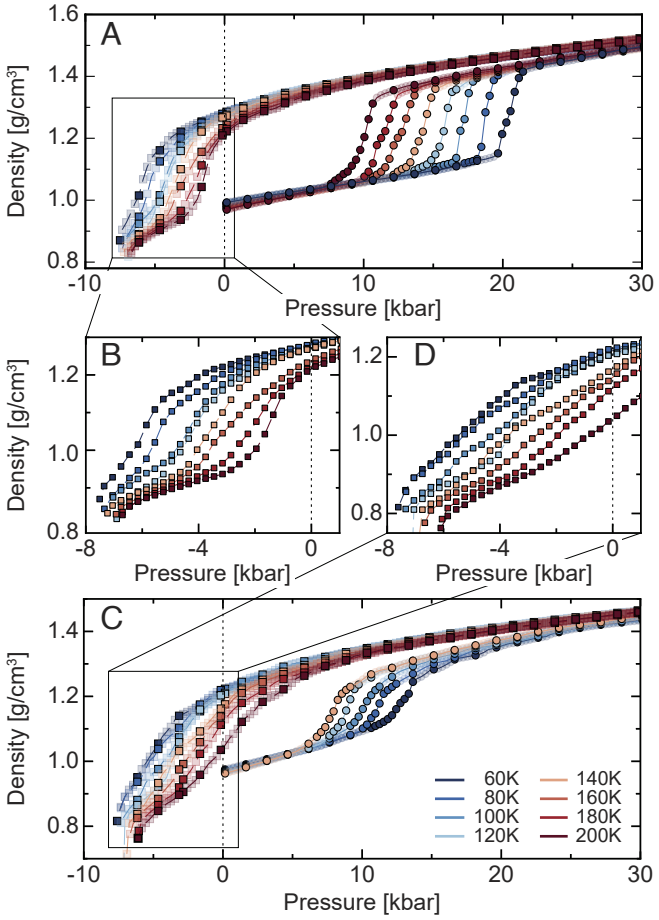

Fig. 4. Density versus pressure isotherms for the compression of LDA to HDA and corresponding decompression to negative pressures. All simulations employ a compression/decompression rate of q_p = 3,000 bar/ns. Panels *A* (full compression and decompression) and *B* (detailed view of decompression and eventual fracture of the glasses) present results for the DP_SCAN model. Panels *C* and *D* present the corresponding results for the DP_MBpol model. Data represent averages over three independent simulations while translucent and solid symbols are used only for visual purposes.

the behavior of the two models investigated here persist under an order of magnitude slower decompression rate q_p = 300 bar/ns.

Fig. 5 shows that the RDFs for HDA predicted by the DP_SCAN and DP_MBpol models are remarkably similar, with the primary difference being a slight shift of the DP_SCAN RDFs toward shorter pair distances, (e.g., the position of the oxygen–oxygen RDF maxima in DP_MBpol and DP_SCAN water differ by $\Delta r \approx 0.03$ Å) This shift is consistent with the higher density of DP_SCAN simulations. When compared to experimental RDFs, the oxygen-hydrogen and hydrogen–hydrogen distributions show good agreement, highlighting the ability of both models to capture the short-range structural features of HDA accurately. However, discrepancies emerge in the oxygen–oxygen RDF, particularly in the 3 to 5 Å region, where the models fail to reproduce the broad second maximum of the experimental RDF. This feature corresponds to a fifth water model protruding from the second solvation shell toward the first. This mismatch persists across all studied water models and suggests a limitation in capturing this aspect of HDA structure (34, 37, 40). It is plausible that the inclusion of nuclear quantum effects could refine the structure and resolve these discrepancies. Additional model refinement to include HDA structures in the training data may also be needed. Moreover, a better understanding of the structural details along the LDA/HDA transition could provide further insight in developing models with enhanced structural fidelity (83–85).

More subtly, our analysis reveals that the recovered HDA RDFs shown in Fig. 5*A* more closely resemble experimental vHDA than HDA. The recovered HDA densities at 1 bar and T = 80 K (1.28 g/cm^3 for DP_SCAN, 1.22 g/cm^3 for DP_MBpol) align closely with experimental vHDA (1.25 g/cm^3) rather than HDA (1.15 g/cm^3) (77, 86). Coordination number analysis supports this interpretation: Both models exhibit approximately 5.6 to 5.8 neighbors within 3.3 Å at 1 bar, consistent with vHDA's characteristic 4+2 coordination (four neighbors in the first shell plus two interstitials) rather than HDA's 4+1 coordination (77).

This apparent discrepancy arises from kinetic effects inherent to simulations. The fast compression and decompression rates used in our simulations (orders of magnitude faster than experimental rates) limit structural relaxation during the pressure cycling process. Consequently, the HDA to LDA transition shifts to progressively more negative pressures than observed experimentally, meaning the system remains in a highly dense state longer during decompression. This kinetic trapping results in correspondingly higher recovered HDA densities at ambient pressure that structurally resemble vHDA rather than the equilibrium HDA observed in experiments. *SI Appendix*, Fig. S8 compares the structure of recovered HDA at 1 bar to both experimental HDA and vHDA and also shows the structure of simulated HDA at the negative pressure where its density matches the experimental value of 1.15 g/cm^3. When this experimental density is reproduced in simulation along the decompression branch, the resulting RDF and coordination number closely match those of experimental HDA.

Fig. 5 *B* and *C* compare the oxygen–oxygen RDFs and structure factors of HDA at T = 80 K and P = 33 kbar, generated via compression of ice Ih and LDA. Notably, the RDFs

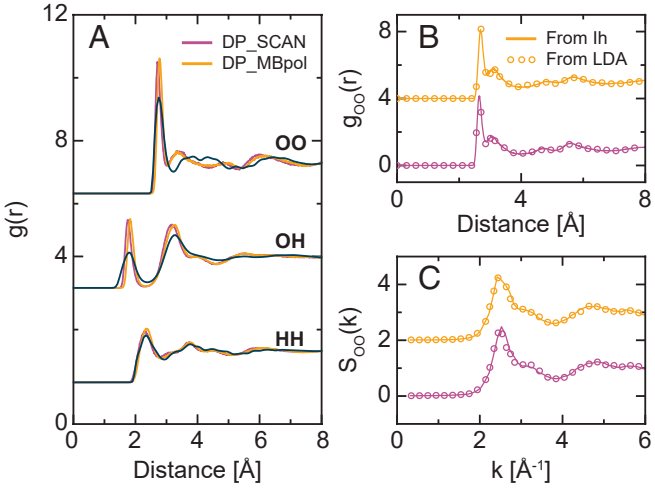

Fig. 5. Structural characterization of HDA. (*A*) Radial distribution functions for oxygen–oxygen, oxygen-hydrogen, and hydrogen–hydrogen pairs, comparing recovered HDA at T = 80 K and ambient pressure generated using the DP_SCAN and DP_MBpol models with experimental data (black line) (77, 78). (*B*) Comparison of oxygen–oxygen RDFs for HDA T = 80 K and P = 33 kbar, generated via compression of hexagonal ice (line) and of LDA (open circles). (*C*) Comparison of oxygen–oxygen structure factors for HDA at T = 80 K and P = 33 kbar, generated via compression of hexagonal ice (line) and of LDA (open circles). Throughout the figure, purple and orange correspond to DP_SCAN and DP_MBpol, respectively.

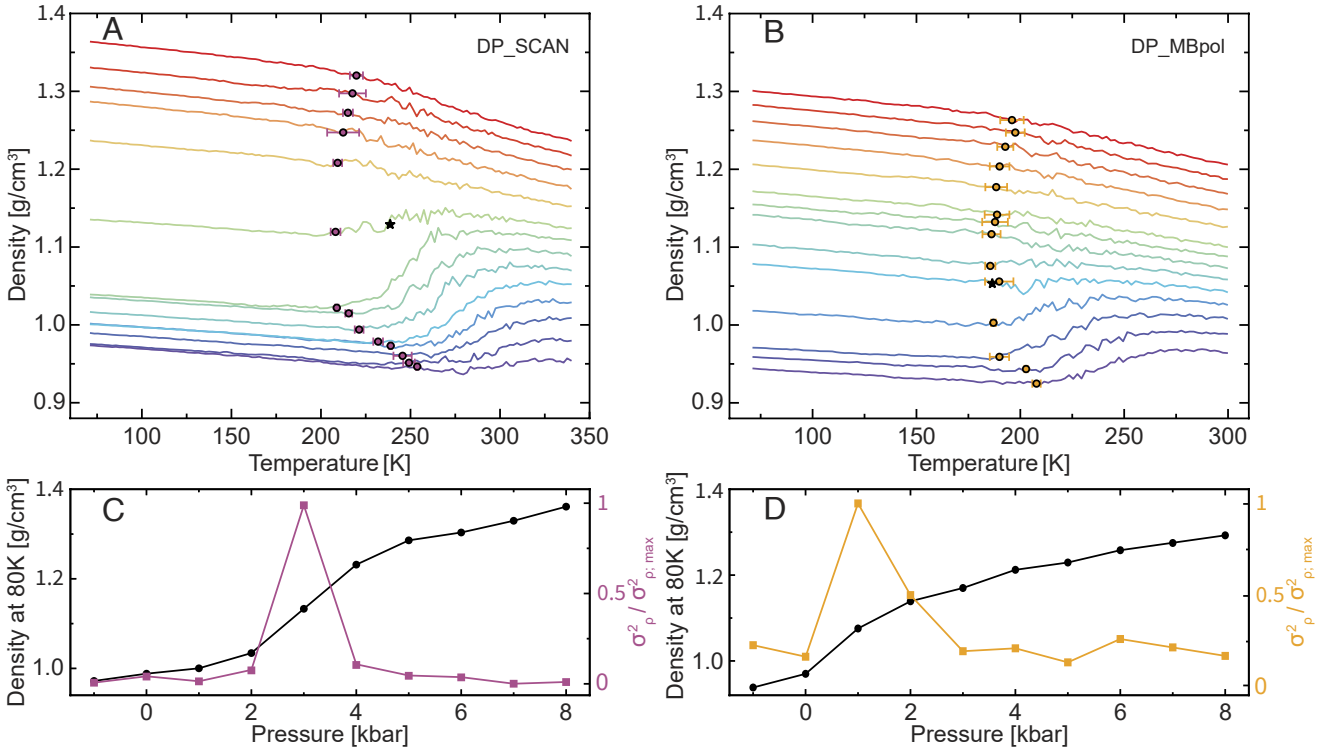

Fig. 6. Characterization of the intermediate ices formed via isobaric quenches. Panels (*A* and *B*) present density versus temperature during isobaric cooling for the DP_SCAN and DP_MBpol models, respectively, at pressures $P = -1{,}000, -500, 1, 500, 1{,}000, 1{,}500, 2{,}000, 2{,}500, 3{,}000, 4{,}000, 5{,}000, 6{,}000, 7{,}000, 8{,}000$ bar (*Bottom* to *Top*) at a cooling rate of $q_c = 10$ K/ns. The circles indicate the glass transition temperatures calculated from a global fit of the enthalpy during cooling and the black stars present the previously reported critical points (61, 91). Panels (*C* and *D*) characterize the glasses as a function of pressure for the DP_SCAN and DP_MBpol model, respectively. The black circles show the average density of the amorphous ices included in (*A* and *B*) at $T = 80$ K while the colored lines quantify the normalized variance in glass density, $\sigma^2_\rho/\sigma^2_{\rho;\,\mathrm{max}}$ across six independent simulations, where $\sigma^2_{\rho;\,\mathrm{max}}$ is defined as the maximum density variance observed across all pressures.

and structure factors are nearly identical regardless of the initial phase, indicating that the HDA phase retains no memory of the initial state, further supporting the robustness of the DP_SCAN and DP_MBpol models in describing the physics of glassy water. Importantly, this agreement is achieved despite neither model being explicitly trained on glassy water states.

A Continuum of Amorphous Ices. Recent experiments by Rosu-Finsen et al. produced an apparently new amorphous phase of ice, called medium-density amorphous ice (MDA), by ball-milling ice Ih at 77 K (24). The recovered MDA density is 1.06 ± 0.06 g/cm^3 and the relationship of this new glassy form to other amorphous ices and its place within the LLPT scenario is not fully understood. Computational studies by Ribeiro et al., which employed the classical atomistic TIP4P/Ice (87) and the machine-learned coarse-grained ML-BOP (88) water models, demonstrated that MDA can be understood as a nonequilibrium steady-state shear-driven amorphous phase, revealing that increasing shear rates at ambient pressure can produce glasses with densities spanning the entire range from LDA to HDA (42). Their simulations further showed that the glasses produced at low shear rates closely resemble glasses obtained by quenching of ambient liquid water. Separately, it has been demonstrated that isobaric quenches at various external pressures with the q-TIP4P/F water model (89) produce a continuum of intermediate amorphous ices (IA), ranging in density from LDA to HDA, passing through the experimentally observed MDA density (90).

We perform isobaric quenches of liquid water at pressures ranging from $P = -1{,}000$ bar to 8,000 bar to investigate the nature of the IAs produced with the DP_SCAN and DP_MBpol models, respectively. Fig. 6 *A* and *B* present density-temperature curves for both models obtained with a cooling rate of $q_c = 10$ K/ns, while *SI Appendix*, Fig S6 provides analogous results for a cooling rate of $q_c = 1$ K/ns, showing very similar trends. The isobars show that by varying the external pressure at which the quench is performed, it is possible to generate IAs with densities ranging from ρ_{LDA} to ρ_{HDA}. Moreover, two distinct regimes of behavior are observed. At low pressures, the liquid proceeds through a density maximum, while at high pressures, the density curves increase monotonically upon cooling.

Fig. 6 *C* and *D* quantitatively capture the differences in the IA obtained by isobaric cooling through two metrics: the IA density at $T = 80$ K (black curves) and the normalized variance, $\sigma^2_\rho/\sigma^2_{\rho;\,\mathrm{max}}$, in this density across six independent simulations (colored curves). The density shows a clear sigmoidal shape, with a transition region centered near 3,000 bar for DP_SCAN and 1,000 bar for DP_MBpol, and a pronounced maximum in glass density variance at these same pressures.

We examine these density variations in the context of water's density maximum anomaly and the LLCP location (92). At ambient pressure, liquid water exhibits a density maximum at $T_{\mathrm{MD}} = 4$ °C. This maximum density exists up to a certain pressure, denoted here as P_{MD}, above which the density increases continuously upon cooling. P_{MD} is slightly larger that the liquid–

liquid critical pressure, P_c (as the density maxima line goes around the LLCP in the $P-T$ plane). Recently, the location of the LLCP for both the DP_SCAN model ($[T_c, P_c]$ = [242 K, 2,950 bar]) and DP_MBpol model ($[T_c, P_c]$ = [188 K, 1,053 bar]) has been calculated (11, 61, 91). Fig. 6 shows that pressures below $P_c \approx P_{MD}$, the density proceeds through a maximum before falling out of equilibrium and the difference between the ρ_{max} and ρ_{min} increases as pressure increases. Conversely, at pressures above $P_c \approx P_{MD}$, the density increases monotonically upon cooling. Due to the spacing between pressures simulated, the density maximum disappears for all pressures $P > P_c$. The glass densities increase linearly upon cooling for all pressures.

Interestingly, both models present a maximum in density variance in the vicinity of the critical pressure, $P \approx P_c$. This reflects enhanced density fluctuations close to criticality, and, together with related observations for the classical TIP4P/2005 and q-TIP4P/F models (47, 90) suggests the experimental study of glasses quenched isobarically across a range of pressures as an interesting avenue for investigating metastable criticality in water. It should, however, be borne in mind when interpreting results such as those shown in Fig. 6 *C* and *D*, that a number of confluent complexities at present stand in the way of simple physical pictures. Such complexities include finite-size effects, glassy dynamics, critical slowing down, and metastability, to name but a few of the factors at play in this region of the phase diagram.

We also calculate the glass transition temperature upon cooling, $T_g(P)$ for each isobar from the enthalpy data, shown as circles Fig. 6 *A* and *B*. The SI outlines a global hyperbolic fitting procedure adapted from Patrone et al. (93) to determine T_g without researcher bias, removing the ambiguity typically introduced by manual selection of linear regions. Clearly, there are two branches of T_g, with differing slopes. Below P_c, T_g values decrease with increasing pressure, while above P_c, they increase with increasing pressure. This bifurcation in T_g behavior provides clear evidence for two distinct amorphous states: LDA-like below P_c and HDA-like above P_c. This matches experimental observations, supporting the LLPT hypothesis and suggesting that the IAs generated without ball milling represent mixtures of LDA and HDA.

Phase Diagrams. Combining our results, we construct out-of-equilibrium "phase diagrams" in the $T-P$ plane. (Fig. 7). We estimate the Ih to HDA, LDA to HDA, and HDA to LDA transition pressures from the compression/decompression runs, as explained above. We use filled symbols for fast compression rate (q_p = 3,000 bar/ns) and open symbols for slower compression rate (q_p = 300 bar/ns) simulations. The transitions shown in Fig. 7 should be considered as spinodals (i.e., stability limits) of the corresponding state (LDA, HDA). The ice Ih to HDA transition remains relatively insensitive to changes in compression rate, while the LDA/HDA transition lines demonstrate a more pronounced rate dependence.

Within the LLPT framework, LDL/HDL spinodal lines (not shown) extend from the LLCP into the glass domain and intersect with the LDA/HDA spinodals at the glass transition temperature (4, 7, 20, 38). Gartner et al. rigorously calculated the location of the DP_SCAN LLCP (purple diamond) and binodal curve (black line) (61), while more recently Sciortino et. al reported the DP_MBpol LLCP (orange diamond) and binodal curve (black curve), which we include in Fig. 7*B* (91). For slower compression rates, the LDA to HDA (up-triangles) and HDA to LDA (down triangles) transformation lines approach each other

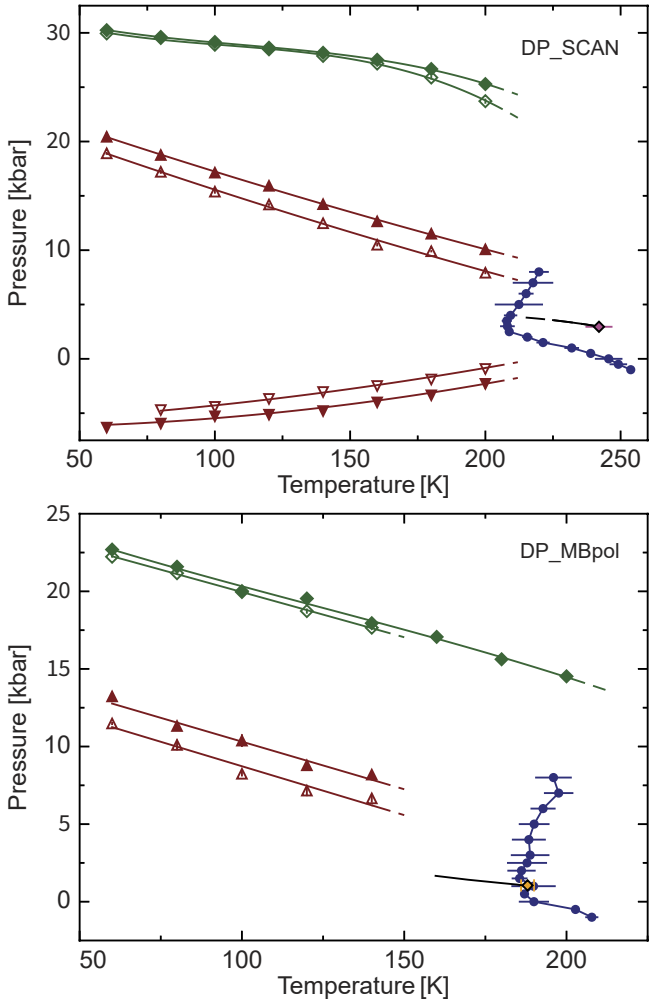

Fig. 7. Nonequilibrium $T-P$ "phase diagrams" of glassy water for the DP_SCAN and DP_MBpol models. Green diamonds indicate pressure induced Ih to HDA transformations; red up- and down-triangles indicate pressure-induced LDA to HDA and HDA to LDA transformations, respectively. Solid and empty symbols correspond to compression/decompression rates of q_p = 3,000 and 300 bar/ns, respectively. The blue circles present T_g calculated from isobaric quenches with a cooling rate of q_c = 10 K/ns. Colored diamonds and the black line show the LLCP and corresponding binodals (61, 91).

and would eventually converge numerically to define the region of LDA/HDA stability. These spinodals would also then terminate at the LLCP, (T_c, P_c).

The features of the DP_SCAN and DP_MBpol phase diagram are qualitatively similar. One marked difference is the absence of HDA to LDA transition temperatures for the DP_MBpol model. This does not indicate that the model lacks this transition. In Fig. 4, the density-pressure curves clearly show a transition from high to low density upon decompression, signifying an HDA to LDA transformation. However, this transition appears smooth at the compression rates we employed, preventing us from estimating a definitive HDA to LDA transition pressure. Further investigation with slower compression rates and/or alternative definitions of the transition temperature would complete this phase diagram.

In Fig. 7, we superimpose the T_g values calculated for each model onto the corresponding phase diagram to compare their positions relative to the critical point and the LDA/HDA spinodals. For the cooling and compression rates employed here, the T_g curve lies well below the critical point for the

DP_SCAN model, while it sits only slightly below the LLCP for the DP_MBpol model. In the T-P plane, we again clearly observe two distinct branches of T_g that transition near the critical pressure, further supporting the viewpoint that the liquid falls out of equilibrium into two different glassy states depending on whether cooling occurs above or below the critical pressure.

Last, we investigate how the compression rate affects the transition pressures. Fig. 8 shows the transition pressures for the pressure-induced Ih to HDA (filled circles) and LDA to HDA (open squares) transition across three orders of magnitude of compression rates, for both models.

The LDA to HDA transition pressures (orange and purple squares) follow a power law relationship with inverse compression rate (*Inset*), $T_P = A \cdot q_p^{-\alpha}$. This fit is used to extrapolate the LDA to HDA transition pressures to the much slower experimental compression rates, originally reported by Mishima et al. (22). The DP_MBpol model extrapolates within 700 bar of the experimental pressure, while the DP_SCAN model overestimates the transition pressure at experimental compression rates by about 2,000 bar. This analysis strongly supports the conclusion that many of the differences between simulation and experimental results stem from the large gap in accessible compression rates. The power law extrapolation demonstrates that both these models can accurately capture experimentally observed behavior when rate effects are accounted for. Notably, Loerting et al. (31) reported that the LDA to HDA transition pressure shows minimal dependence on compression rate over a range spanning 10^{-6} to 10^{-9} bar/ns at $T = 125$ K. This suggests that the transition pressure converges toward the intrinsic stability limit (i.e., the spinodal) at sufficiently slow rates, within experimental uncertainty, whereas the fast simulated rates are significantly away from this limiting behavior.

The rate dependence of the Ih to HDA transition is more difficult to assess. As shown in Fig. 8, it is less pronounced than for the LDA to HDA transition. Furthermore, the negative curvature of the data prevents a reliable extrapolation to experimentally attainable compression rates at this time. However, it is evident that reducing the compression rate will also bring the transition pressure closer to experimental values.

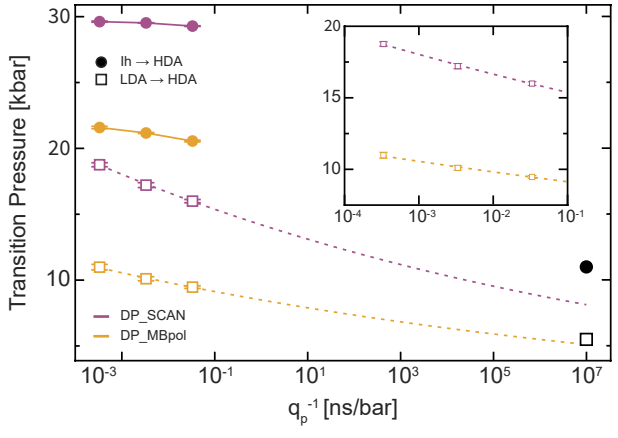

Fig. 8. Compression rate dependence of the calculated transition pressure from Ih to HDA (solid circles) and LDA to HDA (open squares) for isothermal compression simulations at $T = 80$ K. The black symbols indicate the experimental transition pressures (21, 22). The dotted lines correspond to a power law fit, $T_P = A \cdot q_p^{-\alpha}$, over the three simulated compression rates, $q_p =$ 3,000, 300, and 30 bar/ns, extrapolated to the experimental compression rate (21, 22).

Conclusions. We have employed state-of-the-art Deep Potential MLPs to conduct an investigation of water's glassy phenomenology based on DFT and quantum mechanical calculations using the DP_SCAN and DP_MBpol models. The use of DPMD simulations enabled these investigations, as both DFT-SCAN AIMD and direct simulations with MBpol would be computationally prohibitive for the long timescales necessary to study water's glassy states. Despite not being explicitly trained on glassy configurations, both models accurately reproduce the structures and transformations of LDA and HDA, demonstrating that MLPs trained on equilibrium states can effectively model nonequilibrium phenomena.

The comprehensive nonequilibrium "phase diagrams" unify the glassy and liquid domains, revealing how pressure induced glass–glass transformations connect to liquid–liquid spinodals at low temperatures. Our extrapolation across ten orders of magnitude in compression rates brings simulation results into close agreement with experimental transformation pressures. The isobaric quenching simulations across a wide pressure range reveal a connection between metastable criticality and glassy behavior, with enhanced density fluctuations manifesting as maximal variance in glass density near the critical pressure. While further investigation into these results as a function of system size and cooling rates are necessary, they suggest promising experimental approaches for probing liquid–liquid criticality through systematic studies of glasses obtained via quenches near P_c.

The observed bifurcation in glass transition temperature behavior—decreasing with pressure below P_c and increasing above P_c—provides compelling evidence for two distinct amorphous states corresponding to LDA-like and HDA-like behaviors, directly connecting to the underlying liquid–liquid phase transition and supporting the LLPT hypothesis from quantum mechanically derived interaction potentials. Most significantly, our study demonstrates that deep learning approaches preserve the underlying physics of complex water behavior across equilibrium and nonequilibrium regimes without empirical parameterization. Future refinements should address nuclear quantum effects (73) and potentially expand training data to include glassy structures, although our results suggest that rate effects dominate over training set limitations. In summary, this work establishes a comprehensive framework for investigating water's complex polyamorphism with quantum mechanical accuracy, suggests new experiments to probe water's glassy metastability and criticality, and opens broad research avenues for computational investigation with MLPs of metastable molecular states across unprecedented spatiotemporal scales.

Materials and Methods

We performed all MD simulations with both SCAN- and MBpol-based Deep Potential models with the LAMMPS simulation software, version 2 August 2023 (94) patched with the DPMD-kit, version 3.0.0 (51, 54). The DP_SCAN model was previously trained on DFT calculations with the SCAN functional (64), while the DP_MBpol model was trained on the Many-Body Polarizable water model (68). All NPT simulations were done with either 432 (Ih) or 500 (liquid) water molecules. Initial configurations for ice Ih were generated with proton disorder using the GenIce2 (95) package, while liquid configurations were generated by the Gromacs version 2019.6 (96) insert-molecules tool before subsequent equilibration. Temperature and pressure were maintained using the LAMMPS Nosé–Hoover thermostat and barostat with a relaxation time of 0.5 ps. To aid in the computational effort, we used a hydrogen mass of 2 atomic mass units which enabled a simulation time step of 0.5 fs, but we employed a molar mass of 18 g/mol for analysis. To demonstrate this method's efficacy, we provide simulation

results in *SI Appendix*, Fig. S7 which employed a hydrogen mass of 1 amu and a time step of 0.25 fs.

Data, Materials, and Software Availability. Simulation data, analysis scripts, and code to generate figures have been deposited in and available for download at Princeton Data Commons (https://datacommons.princeton.edu/discovery/catalog/doi-10-34770-a0v3-ye51) (97).

ACKNOWLEDGMENTS. R.J.S. and P.G.D. acknowledge support from the "Chemistry in Solution and at Interfaces" Center funded by the U.S. Department of Energy through Award No. DE-SC0019394. Simulations and analyses were performed using resources from Princeton Research Computing at Princeton University, which is a consortium led by the Princeton Institute for Computational Science and Engineering and Office of Information Technology's Research Computing. N.G. is thankful to the NSF (grant No. CHE-2223461) and to the NSF-CREST Center for Interface Design and Engineered Assembly of Low Dimensional systems IDEALS grant numbers HRD-1547380 and HRD-2112550.

Author affiliations: [a]Department of Chemistry, Princeton University, Princeton, NJ 08544; [b]Department of Physics, Brooklyn College of the City, University of New York, Brooklyn, NY 11210; and [c]Department of Chemical and Biological Engineering, Princeton University, Princeton, NJ 08544

1. D. Eisenberg, W. Kauzmann, *The Structure and Properties of Water* (Oxford University Press, USA, 2005).
2. R. J. Speedy, Isothermal compressibility of supercooled water and evidence for a thermodynamic singularity at −45°C. *J. Chem. Phys.* **65**, 851–858 (1976).
3. H. E. Stanley *et al*., The puzzling behavior of water at very low temperature. Invited lecture. *Phys. Chem. Chem. Phys.* **2**, 1551–1558 (2000).
4. P. G. Debenedetti, *Metastable Liquids: Concepts and Principles* (Princeton University Press, 2020).
5. R. J. Speedy, Stability-limit conjecture. An interpretation of the properties of water. *J. Chem. Phys.* **86**, 982–991 (1982).
6. S. Sastry, P. G. Debenedetti, F. Sciortino, H. E. Stanley, Singularity-free interpretation of the thermodynamics of supercooled water. *Phys. Rev. E* **53**, 6144 (1996).
7. P. H. Poole, F. Sciortino, U. Essmann, H. E. Stanley, Phase behaviour of metastable water. *Nature* **360**, 324–328 (1992).
8. Y. Liu, J. C. Palmer, A. Z. Panagiotopoulos, P. G. Debenedetti, Liquid-liquid transition in ST2 water. *J. Chem. Phys.* **137**, 214505 (2012).
9. J. C. Palmer *et al*., Metastable liquid-liquid transition in a molecular model of water. *Nature* **510**, 385–388 (2014).
10. P. G. Debenedetti, F. Sciortino, G. H. Zerze, Second critical point in two realistic models of water. *Science* **369**, 289–292 (2020).
11. T. E. Gartner III *et al*., Signatures of a liquid-liquid transition in an ab initio deep neural network model for water. *Proc. Natl. Acad. Sci. U.S.A.* **117**, 26040–26046 (2020).
12. L. E. Coronas, G. Franzese, Phase behavior of metastable water from large-scale simulations of a quantitatively accurate model near ambient conditions: The liquid-liquid critical point. *J. Chem. Phys.* **161**, 164502 (2024).
13. K. H. Kim *et al*., Experimental observation of the liquid-liquid transition in bulk supercooled water under pressure. *Science* **370**, 978–982 (2020).
14. L. Kringle, W. A. Thornley, B. D. Kay, G. A. Kimmel, Reversible structural transformations in supercooled liquid water from 135 to 245 K. *Science* **369**, 1490–1492 (2020).
15. N. Giovambattista, P. H. Poole, Liquid-liquid phase transition in simulations of ultrafast heating and decompression of amorphous ice. *J. Non Cryst. Solids* **11**, 100067 (2021).
16. A. Nilsson, Origin of the anomalous properties in supercooled water based on experimental probing inside "no-man's land". *J. Non Cryst. Solids* **14**, 100095 (2022).
17. Y. Suzuki, Direct observation of reversible liquid-liquid transition in a trehalose aqueous solution. *Proc. Natl. Acad. Sci. U.S.A.* **119**, e2113411119 (2022).
18. K. Amann-Winkel *et al*., Liquid-liquid phase separation in supercooled water from ultrafast heating of low-density amorphous ice. *Nat. Commun.* **14**, 442 (2023).
19. K. Winkel, E. Mayer, T. Loerting, Equilibrated high-density amorphous ice and its first-order transition to the low-density form. *J. Phys. Chem. B* **115**, 14141–14148 (2011).
20. O. Mishima, H. E. Stanley, The relationship between liquid, supercooled and glassy water. *Nature* **396**, 329–335 (1998).
21. O. Mishima, L. Calvert, E. Whalley, 'melting ice'I at 77 K and 10 kbar: A new method of making amorphous solids. *Nature* **310**, 393–395 (1984).
22. O. Mishima, L. Calvert, E. Whalley, An apparently first-order transition between two amorphous phases of ice induced by pressure. *Nature* **314**, 76–78 (1985).
23. T. Loerting, C. Salzmann, I. Kohl, E. Mayer, A. Hallbrucker, A second distinct structural "state" of high-density amorphous ice at 77 K and 1 bar. *Phys. Chem. Chem. Phys.* **3**, 5355–5357 (2001).
24. A. Rosu-Finsen *et al*., Medium-density amorphous ice. *Science* **379**, 474–478 (2023).
25. E. Burton, W. Oliver, X-ray diffraction patterns of ice. *Nature* **135**, 505–506 (1935).
26. E. Mayer, New method for vitrifying water and other liquids by rapid cooling of their aerosols. *J. Appl. Phys.* **58**, 663–667 (1985).
27. J. Bachler, J. Giebelmann, T. Loerting, Experimental evidence for glass polymorphism in vitrified water droplets. *Proc. Natl. Acad. Sci. U.S.A.* **118**, e2108194118 (2021).
28. P. H. Handle, T. Loerting, Temperature-induced amorphisation of hexagonal ice. *Phys. Chem. Chem. Phys.* **17**, 5403–5412 (2015).
29. O. Mishima, Y. Suzuki, Vitrification of emulsified liquid water under pressure. *J. Chem. Phys.* **115**, 4199–4202 (2001).
30. S. Klotz *et al*., Nature of the polyamorphic transition in ice under pressure. *Phys. Rev. Lett.* **94**, 025506 (2005).
31. T. Loerting *et al*., Amorphous ice: Stepwise formation of very-high-density amorphous ice from low-density amorphous ice at 125 K. *Phys. Rev. Lett.* **96**, 025702 (2006).
32. P. Gallo *et al*., Water: A tale of two liquids. *Chem. Rev.* **116**, 7463–7500 (2016).
33. P. H. Handle, T. Loerting, F. Sciortino, Supercooled and glassy water: Metastable liquid (s), amorphous solid (s), and a no-man's land. *Proc. Natl. Acad. Sci. U.S.A.* **114**, 13336–13344 (2017).
34. J. Chiu, F. W. Starr, N. Giovambattista, Pressure-induced transformations in computer simulations of glassy water. *J. Chem. Phys.* **139**, 184504 (2013).
35. J. Chiu, F. W. Starr, N. Giovambattista, Heating-induced glass-glass and glass-liquid transformations in computer simulations of water. *J. Chem. Phys.* **140**, 114504 (2014).
36. N. Giovambattista, F. Sciortino, F. W. Starr, P. H. Poole, Potential energy landscape of the apparent first-order phase transition between low-density and high-density amorphous ice. *J. Chem. Phys.* **145**, 224501 (2016).
37. J. Wong, D. A. Jahn, N. Giovambattista, Pressure-induced transformations in glassy water: A computer simulation study using the TIP4P/2005 model. *J. Chem. Phys.* **143**, 074501 (2015).
38. J. Engstler, N. Giovambattista, Heating-and pressure-induced transformations in amorphous and hexagonal ice: A computer simulation study using the TIP4P/2005 model. *J. Chem. Phys.* **147**, 074505 (2017).
39. P. H. Handle, F. Sciortino, N. Giovambattista, Glass polymorphism in TIP4P/2005 water: A description based on the potential energy landscape formalism. *J. Chem. Phys.* **150**, 244506 (2019).
40. N. Giovambattista, H. Eugene Stanley, F. Sciortino, Phase diagram of amorphous solid water: Low-density, high-density, and very-high-density amorphous ices. *Phys. Rev. E* **72**, 031510 (2005).
41. D. Dhabal, V. Molinero, Kinetics and mechanisms of pressure-induced ice amorphization and polyamorphic transitions in a machine-learned coarse-grained water model. *J. Phys. Chem. B* **127**, 2847–2862 (2023).
42. I. de Almeida Ribeiro *et al*., Medium-density amorphous ice unveils shear rate as a new dimension in water's phase diagram. *Proc. Natl. Acad. Sci. U.S.A.* **121**, e2414444121 (2024).
43. N. Zorzi, A. Neophytou, F. Sciortino, Two state model for the ML-BOP potential. *Mol. Phys.* **122**, e2407025 (2024).
44. A. Neophytou, F. Sciortino, Potential energy landscape of a coarse grained model for water: ML-BOP. *J. Chem. Phys.* **160**, 114502 (2024).
45. N. Giovambattista, T. Loerting, B. R. Lukanov, F. W. Starr, Interplay of the glass transition and the liquid-liquid phase transition in water. *Sci. Rep.* **2**, 390 (2012).
46. M. Seidl *et al*., Volumetric study consistent with a glass-to-liquid transition in amorphous ices under pressure. *Phys. Rev. B* **83**, 100201 (2011).
47. T. E. Gartner III, S. Torquato, R. Car, P. G. Debenedetti, Manifestations of metastable criticality in the long-range structure of model water glasses. *Nat. Commun.* **12**, 3398 (2021).
48. R. Car, M. Parrinello, Unified approach for molecular dynamics and density-functional theory. *Phys. Rev. Lett.* **55**, 2471 (1985).
49. J. Hutter, Car-Parrinello molecular dynamics. *Wiley Interdiscip. Rev. Comput. Mol. Sci.* **2**, 604–612 (2012).
50. J. Behler, M. Parrinello, Generalized neural-network representation of high-dimensional potential-energy surfaces. *Phys. Rev. Lett.* **98**, 146401 (2007).
51. L. Zhang, J. Han, H. Wang, R. Car, E. Weinan, Deep potential molecular dynamics: A scalable model with the accuracy of quantum mechanics. *Phys. Rev. Lett.* **120**, 143001 (2018).
52. P. Friederich, F. Häse, J. Proppe, A. Aspuru-Guzik, Machine-learned potentials for next-generation matter simulations. *Nat. Mater.* **20**, 750–761 (2021).
53. A. Omranpour, P. Montero De Hijes, J. Behler, C. Dellago, Perspective: Atomistic simulations of water and aqueous systems with machine learning potentials. *J. Chem. Phys.* **160**, 170901 (2024).
54. H. Wang, L. Zhang, J. Han, E. Weinan, DeePMD-kit: A deep learning package for many-body potential energy representation and molecular dynamics. *Comput. Phys. Commun.* **228**, 178–184 (2018).
55. T. Wen, L. Zhang, H. Wang, E. Weinan, D. J. Srolovitz, Deep potentials for materials science. *Mater. Futur.* **1**, 022601 (2022).
56. J. Sun, A. Ruzsinszky, J. P. Perdew, Strongly constrained and appropriately normed semilocal density functional. *Phys. Rev. Lett.* **115**, 036402 (2015).
57. M. Chen *et al*., Ab initio theory and modeling of water. *Proc. Natl. Acad. Sci. U.S.A.* **114**, 10846–10851 (2017).
58. C. Zhang *et al*., Modeling liquid water by climbing up Jacob's ladder in density functional theory facilitated by using deep neural network potentials. *J. Phys. Chem. B* **125**, 11444–11456 (2021).
59. P. M. Piaggi, A. Z. Panagiotopoulos, P. G. Debenedetti, R. Car, Phase equilibrium of water with hexagonal and cubic ice using the scan functional. *J. Chem. Theory Comput.* **17**, 3065–3077 (2021).
60. P. M. Piaggi, J. Weis, A. Z. Panagiotopoulos, P. G. Debenedetti, R. Car, Homogeneous ice nucleation in an ab initio machine-learning model of water. *Proc. Natl. Acad. Sci. U.S.A.* **119**, e2207294119 (2022).
61. T. E. Gartner III, P. M. Piaggi, R. Car, A. Z. Panagiotopoulos, P. G. Debenedetti, Liquid-liquid transition in water from first principles. *Phys. Rev. E* **129**, 255702 (2022).
62. I. Sanchez-Burgos, M. C. Muniz, J. R. Espinosa, A. Z. Panagiotopoulos, A deep potential model for liquid-vapor equilibrium and cavitation rates of water. *J. Chem. Phys.* **158**, 184504 (2023).
63. M. Calegari Andrade, R. Car, A. Selloni, Probing the self-ionization of liquid water with ab initio deep potential molecular dynamics. *Proc. Natl. Acad. Sci. U.S.A.* **120**, e2302468120 (2023).
64. L. Zhang, H. Wang, R. Car, E. Weinan, Phase diagram of a deep potential water model. *Phys. Rev. Lett.* **126**, 236001 (2021).
65. V. Babin, C. Leforestier, F. Paesani, Development of a "first principles" water potential with flexible monomers: Dimer potential energy surface, VRT spectrum, and second virial coefficient. *J. Chem. Theory Comput.* **9**, 5395–5403 (2013).
66. V. Babin, G. R. Medders, F. Paesani, Development of a "first principles" water potential with flexible monomers. II: Trimer potential energy surface, third virial coefficient, and small clusters. *J. Chem. Theory Comput.* **10**, 1599–1607 (2014).
67. G. R. Medders, V. Babin, F. Paesani, Development of a "first-principles" water potential with flexible monomers. III. Liquid phase properties. *J. Chem. Theory Comput.* **10**, 2906–2910 (2014).

68. S. L. Bore, F. Paesani, Realistic phase diagram of water from "first principles" data-driven quantum simulations. *Nat. Commun.* **14**, 3349 (2023).
69. I. Kohl, L. Bachmann, A. Hallbrucker, E. Mayer, T. Loerting, Liquid-like relaxation in hyperquenched water at $\leq$ 140 K. *Phys. Chem. Chem. Phys.* **7**, 3210–3220 (2005).
70. K. Röttger, A. Endriss, J. Ihringer, S. Doyle, W. Kuhs, Lattice constants and thermal expansion of h_2o and d_2o ice ih between 10 and 265 K. *Struct. Sci.* **50**, 644–648 (1994).
71. T. Loerting *et al*., Cryoflotation: Densities of amorphous and crystalline ices. *J. Phys. Chem. B* **115**, 14167–14175 (2011).
72. A. Eltareb, G. E. Lopez, N. Giovambattista, The importance of nuclear quantum effects on the thermodynamic and structural properties of low-density amorphous ice: A comparison with hexagonal ice. *J. Phys. Chem. B* **127**, 4633–4645 (2023).
73. A. Eltareb, B. A. Khan, G. E. Lopez, N. Giovambattista, Nuclear quantum effects on glassy water under pressure: Vitrification and pressure-induced transformations. *J. Chem. Phys.* **161**, 234502 (2024).
74. P. L. Chau, A. J. Hardwick, A new order parameter for tetrahedral configurations. *Mol. Phys.* **93**, 511–518 (1998).
75. J. R. Errington, P. G. Debenedetti, Relationship between structural order and the anomalies of liquid water. *Nature* **409**, 318–321 (2001).
76. P. J. Linstrom, W. G. Mallard, NIST chemistry WebBook, NIST standard reference database number 69. https://www.nist.gov/srd. Accessed 15 May 2025.
77. J. Finney, A. Hallbrucker, I. Kohl, A. Soper, D. Bowron, Structures of high and low density amorphous ice by neutron diffraction. *Phys. Rev. Lett.* **88**, 225503 (2002).
78. D. Mariedahl *et al*., X-ray scattering and O-O pair-distribution functions of amorphous ices. *J. Phys. Chem. B* **122**, 7616–7624 (2018).
79. D. Reisman *et al*., Pulsed power accelerator for material physics experiments. *PRAB* **18**, 090401 (2015).
80. D. Dolan, Y. Gupta, Time-dependent freezing of water under dynamic compression. *Chem. Phys. Lett.* **374**, 608–612 (2003).
81. M. Marshall *et al*., Metastability of liquid water freezing into ice VII under dynamic compression. *Phys. Rev. Lett.* **127**, 135701 (2021).
82. O. Mishima, Relationship between melting and amorphization of ice. *Nature* **384**, 546–549 (1996).
83. Y. A. Gutiérrez Fosado, D. Michieletto, F. Martelli, Link to densify: Topological transitions and origin of hysteresis during the compression and decompression of amorphous ices. *Phys. Rev. Lett.* **133**, 266102 (2024).
84. F. Martelli, F. Leoni, F. Sciortino, J. Russo, Connection between liquid and non-crystalline solid phases in water. *J. Chem. Phys.* **153**, 104503 (2020).
85. G. Ramesh, V. Mahajan, D. Koner, R. S. Singh, Microscopic pathways of transition from low-density to high-density amorphous phase of water. *J. Chem. Phys.* **160**, 194501 (2024).
86. K. Amann-Winkel, D. T. Bowron, T. Loerting, Structural differences between unannealed and expanded high-density amorphous ice based on isotope substitution neutron diffraction. *Mol. Phys.* **117**, 3207–3216 (2019).
87. J. Abascal, E. Sanz, R. García Fernández, C. Vega, A potential model for the study of ices and amorphous water: TIP4P/ice. *J. Chem. Phys.* **122**, 234511 (2005).
88. H. Chan *et al*., Machine learning coarse grained models for water. *Nat. Commun.* **10**, 379 (2019).
89. S. Habershon, T. E. Markland, D. E. Manolopoulos, Competing quantum effects in the dynamics of a flexible water model. *J. Chem. Phys.* **131**, 024501 (2009).
90. A. Eltareb, G. E. Lopez, N. Giovambattista, A continuum of amorphous ices between low-density and high-density amorphous ice. *Commun. Chem.* **7**, 36 (2024).
91. F. Sciortino, Y. Zhai, S. Bore, F. Paesani, Constraints on the location of the liquid-liquid critical point in water. *Nat. Phys.* **21**, 1–6 (2025).
92. F. Sciortino, Multitude of glasses of water. *Proc. Natl. Acad. Sci. U.S.A.* **122**, e2423093121 (2025).
93. P. N. Patrone, A. Dienstfrey, A. R. Browning, S. Tucker, S. Christensen, Uncertainty quantification in molecular dynamics studies of the glass transition temperature. *Polymer* **87**, 246–259 (2016).
94. A. P. Thompson *et al*., LAMMPS-a flexible simulation tool for particle-based materials modeling at the atomic, meso, and continuum scales. *Comput. Phys. Commun.* **271**, 108171 (2022).
95. M. Matsumoto, T. Yagasaki, H. Tanaka, GenIce: Hydrogen-disordered ice generator. *J. Comput. Chem.* **39**, 61–64 (2018).
96. M. J. Abraham *et al*., GROMACS: High performance molecular simulations through multi-level parallelism from laptops to supercomputers. *SoftwareX* **1**, 19–25 (2015).
97. R. J. Szukalo et al., Data from "Computational investigation of water glasses using machine-learning potentials." Princeton Data Commons. https://datacommons.princeton.edu/discovery/catalog/doi-10-34770-a0v3-ye51. Deposited 1 July 2025.